



# Spectral focusing-based stimulated Raman scattering microscopy using compact glass blocks for adjustable dispersion

JUSTIN R. GAGNON,<sup>1,†</sup> CHRISTIAN HARRY ALLEN,<sup>1,†</sup>  DOMINIQUE TRUDEL,<sup>2,3,4</sup> FREDERIC LEBLOND,<sup>2,3,5</sup> PETER K. STYS,<sup>6</sup> CRAIG BRIDEAU,<sup>6</sup>  AND SANGEETA MURUGKAR<sup>1,\*</sup> 

<sup>1</sup>Department of Physics, Carleton University, 1125 Colonel By Drive, Ottawa, Ontario, K1S 5B6, Canada

<sup>2</sup>Centre de recherche du Centre hospitalier de l'Université de Montréal, Montreal, Quebec, Canada

<sup>3</sup>Institut du cancer de Montréal, Montreal, Quebec, Canada

<sup>4</sup>Department of Pathology and cellular Biology, Université de Montréal 2900, boulevard Édouard-Montpetit, Montreal, Quebec, Canada

<sup>5</sup>Department of Engineering Physics, Polytechnique Montréal, 2500 chemin de Polytechnique, Montreal, Quebec, Canada

<sup>6</sup>Department of Clinical Neurosciences, University of Calgary, 3330 Hospital Drive N.W. HRIC 1B37A, Calgary, Alberta, T2N 4N1, Canada

<sup>†</sup>Contributed equally to this work.

\*smurugkar@physics.carleton.ca

**Abstract:** Spectral focusing is a well-established technique for increasing spectral resolution in coherent Raman scattering microscopy. However, current methods for tuning optical chirp in setups using spectral focusing, such as glass rods, gratings, and prisms, are very cumbersome, time-consuming to use, and difficult to align, all of which limit more widespread use of the spectral focusing technique. Here, we report a stimulated Raman scattering (SRS) configuration which can rapidly tune optical chirp by utilizing compact adjustable-dispersion TIH53 glass blocks. By varying the height of the blocks, the number of bounces in the blocks and therefore path length of the pulses through the glass can be quickly modulated, allowing for a convenient method of adjusting chirp with almost no necessary realignment. To demonstrate the flexibility of this configuration, we characterize our system's signal-to-noise ratio and spectral resolution at different chirp values and perform imaging in both the carbon-hydrogen stretching region (MCF-7 cells) and fingerprint region (prostate cores). Our findings show that adjustable-dispersion glass blocks allow the user to effortlessly modify their optical system to suit their imaging requirements. These blocks can be used to significantly simplify and miniaturize experimental configurations utilizing spectral focusing.

© 2023 Optica Publishing Group under the terms of the [Optica Open Access Publishing Agreement](#)

## 1. Introduction

Stimulated Raman scattering (SRS) microscopy is a powerful chemical imaging technique [1,2] that has been applied to a diverse array of applications in recent years including virtual histology [3,4], *in vitro* [5–7], and *in vivo* [8–10] biological imaging. It has been implemented using a variety of laser sources where the pump and Stokes laser pulses are both narrowband picosecond pulses [4,8], broadband and narrowband pulses [11,12], or both broadband femtosecond pulses [13,14]. Stimulated Raman scattering microscopy when implemented using broadband femtosecond laser pulses commonly utilizes the spectral focusing method [13,15–20]. This involves changing the temporal delay between both excitation (pump and Stokes) laser pulses after appropriate chirping so that the instantaneous frequency difference matches that of the target Raman band. Modifying the chirp of an optical system commonly entails substituting many different lengths of glass rods to modulate the pulse chirp for both the pump and Stokes pulses [21]. However, substituting

glass rods in this manner can be time-consuming and can necessitate realigning the entire optical system. Furthermore, the multiple lengths of glass rods (up to 60 cm for a spectral resolution of  $20\text{--}25\text{ cm}^{-1}$ ) [21] can be quite cumbersome to swap in an optical configuration and are not well-suited for developing compact miniaturized setups. While it is also possible to provide tunable linear chirp by using a grating pair or prisms, these tend to be even harder to align and accrue a large amount of third-order dispersion and spatial chirp from even slight misalignments [19].

Here, we present an experimental configuration that makes use of flexible and compact ( $35 \times 60 \times 70\text{ mm}^3$ ) adjustable-dispersion TIH53 glass blocks and tackles the issue of chirp modulation in spectral focusing setups. These blocks were developed to enable compact and tunable chirping of near-infrared (NIR) femtosecond lasers for coherent anti-Stokes Raman scattering (CARS) imaging [22,23]. The blocks employ two parallel internally mirrored surfaces to recirculate the beam for multiple passes. A novel angled exit ramp allows the user to select the total number of passes by translating the block at normal incidence rather than requiring an angular adjustment. The design of the block and exit prisms was completed at the University of Calgary [22,23] with reflective geometry and dispersion calculations to estimate the second- and third-order dispersion achieved with various numbers of bounces within the prism. The final design was manufactured by BMV Optical in Ottawa, Canada, who cut, polished, and coated the prisms with mirror and anti-reflective coatings on the reciprocating and entrance/exit surfaces respectively. By selecting the number of bounces in these glass blocks, the length of propagation within the TIH53 glass can be varied, allowing for the ability to tune the chirp of the pulses without substantially altering the optical alignment. Furthermore, by increasing or decreasing the amount of chirp, the spectral resolution of the interaction can be tuned, trading off the increased peak power of shorter chirped pulses for the spectral resolution gained by increased chirped pulses or vice-versa. We characterized the performance of our SRS microscopy setup when using different values for the chirp of the pump and Stokes pulses utilizing the adjustable-dispersion glass block. To this effect, we measured the signal-to-noise ratio (SNR) and spectral resolution as a function of the number of bounces in the glass blocks, exploiting the ease of chirp modulation to probe both the fingerprint (FP) and carbon-hydrogen stretching (CH) spectral regions. We demonstrate our system's capabilities by imaging biological samples. In the FP region, we image prostate cancer samples at  $1004$ ,  $1250$ ,  $1477$ , and  $1644\text{ cm}^{-1}$ , corresponding to Raman band contributions from phenylalanine, adenine/guanine, and lipids respectively. In the CH region, we image MCF-7 breast cancer cells at  $2850\text{ cm}^{-1}$  corresponding to lipids and  $2926\text{ cm}^{-1}$  with overlapping contributions from proteins, lipids, and DNA. Our results demonstrate that our adjustable-dispersion TIH53 glass blocks offer a quick and compact alternative to modulate the chirp of spectral focusing setups to suit imaging requirements.

## 2. Experimental setup

### 2.1. Compact glass block for adjustable dispersion

TIH53 glass is used in the glass block due to its high refractive index, as well as high transmittance and high group velocity dispersion (GVD) to third-order dispersion (TOD) ratio at the wavelengths used in this experiment [22]. The  $35 \times 60 \times 70\text{ mm}^3$  glass block has one side mirrored with silver, with the opposite side having a transparent ramp from which the beam exits the block (Fig. 1). A silver mirror surface above the ramp reflects the beam back and forth until reaching the transparent ramp edge. The amount of glass propagated by the beam can therefore be modulated by the number of reflections inside the block. The number of reflections can be changed by varying the height of the block, which adjusts the net horizontal distance  $L$  required to reach the transparent surface at the exit. A vertical distance of  $2.5\text{ mm}$  is required to adjust from one bounce to the next without clipping. The length  $L$  within the blocks controls the group delay dispersion (GDD) values, and hence the pulse duration (see Supplement 1). This length is

composed of a propagation distance of 10 cm for each bounce due to the 5 cm distance between the silver mirrored surfaces, plus an additional distance of 6 cm in the glass from the entry surface to the transparent ramp side before exiting. The glass block can admit up to 12 bounces for a maximum of 126 cm of propagation within TIH53 glass, corresponding to a maximum estimated GDD of 279000 fs<sup>2</sup> at 796 nm, 215000 fs<sup>2</sup> at 942 nm, and 183000 fs<sup>2</sup> at 1040 nm. To prevent spatial chirp, the beam enters the glass block at normal incidence. The silver mirrored surfaces are then angled in relation to the glass surfaces so that the beam may propagate by reflecting internally throughout the glass block.

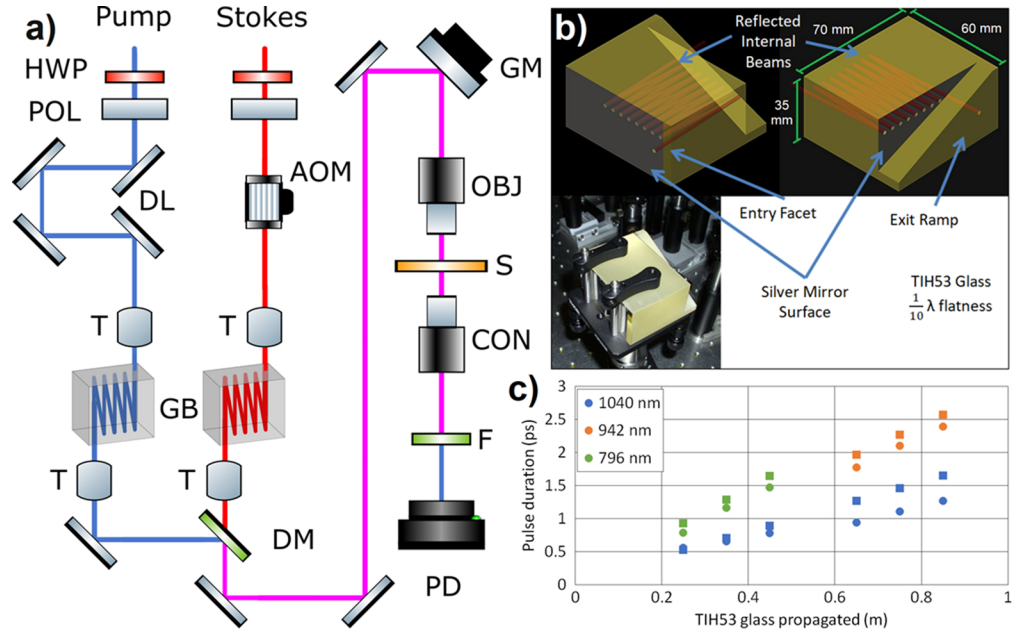


**Fig. 1.** Spectral focusing SRS microscopy using compact TIH53 glass blocks. **(a)** Schematic of setup. HWP: Half-wave plate; POL: Polarizer; AOM: Acousto-optic modulator; DL: Delay line; T: Telescope; GB: Glass block; DM: Dichroic mirror; GM: Galvanometer mirrors; OBJ: Objective; S: Sample; CON: Condenser; F: Filter; PD: Photodetector. **(b)** Schematic (top) and photo (bottom left) of the adjustable-dispersion TIH53 glass block. The beam enters the block, bounces between the two silver mirrors, and exits from an unsilvered ramp. **(c)** Experimentally determined pulse durations (circle) versus theoretical predictions (square).

The Raman linewidth ranges from a few wavenumbers in the FP region to  $\sim 100 \text{ cm}^{-1}$  for lipids in the CH region [24]. To target these spectral resolution values, assuming a Gaussian pulse shape for the transform-limited pump and Stokes pulses, the estimated number of bounces in each of the glass blocks to satisfy the desired chirp-matching conditions is required to be in the range of 6–8 for the FP region and 2–4 in the CH regions (see Supplement 1). In this work, the number of bounces in both the pump and Stokes glass blocks was made identical to maintain an approximately constant chirp ratio at different bounce number settings.

## 2.2. SRS microscopy with compact glass blocks

Our multimodal SRS imaging platform consists of a dual output 80 MHz Ti:Sapphire pumped optical parametric oscillator system (Insight DS+, MKS) [25]. The Stokes output ( $\sim 200 \text{ fs}$ ) is fixed at 1040 nm, while the pump output ( $\sim 130 \text{ fs}$ ) is tunable between 680–1300 nm. Figure 1(a) shows a schematic of the spectral focusing SRS microscopy setup using the adjustable-dispersion

glass blocks. The pump and Stokes beams both initially pass through a combination of a half-wave plate (HWP) and polarizer (POL) that function as a power controller. The Stokes pulses traverse an acousto-optic modulator (AOM, Isomet 120C5-2) which imparts a ~5 MHz modulation, and they are then chirped in the adjustable-dispersion glass blocks (CB). The pump pulses pass through an adjustable delay line (DL, Zaber X-LDM110C-AE54) to modulate the temporal overlap of the pulses and are then chirped in another glass block. The pump and Stokes beams are magnified to a collimated beam diameter of 1 mm using telescopes to ensure that the beams are not clipped by the glass blocks. The glass blocks are mounted on a z-stage (Thorlabs LJ750/M) to modulate the height of the blocks. Since the beam exits the glass block at a different horizontal position when adding a bounce, a mirror following the glass block is mounted on a sliding stage that moves the mirror horizontally to compensate for the beam offset. After the glass blocks, another telescope is used in each arm to resize the beam so that it slightly overfills the back-aperture of the microscope objective (OBJ). Once the pump and Stokes beams are combined with a dichroic combiner mirror (DM), they are scanned by galvanometer mirrors (GM) and focused with the microscope objective onto the sample (S) in the *xy*-plane to yield an image. Two different objectives are used: a 0.8 NA 40X water immersion objective (Olympus 1-U2M587) for immersed samples, and a 0.75 NA 20X air objective (Olympus 1-U2B825) for samples on slides. The resulting SRS signal is collimated by a 1.25 NA oil condenser (CON) and the Stokes beam is filtered with a long-pass filter (F, Thorlabs FESH1000 + Chroma ET825/150) so a photodiode (PD, Thorlabs FDS1010) can collect the pump light for subsequent analysis with a lock-in amplifier (Zurich instruments MFLI) to determine the stimulated Raman loss signal. To generate the SRS images, powers of 50 mW and 30 mW are used for the pump and Stokes respectively, with a pixel dwell time of 20  $\mu$ s. ScanImage (Version 5.6, Vidrio Technologies) [26] was used for control of the laser scanning and image acquisition.

### 2.3. SRS imaging setup characterization

**Pulse duration** The pulse durations for the pump and Stokes were experimentally obtained via a method by Piazza et al. [27]. The sum-frequency generation (SFG) and the non-resonant four-wave mixing (FWM) signals were generated in a 50  $\mu$ m thick beta barium borate (BBO) crystal (Eksma Optics, BBO-600 H) by the overlapping pump and Stokes pulses. The intensity profiles of the SFG and FWM spectra were collected by scanning the delay line to vary the relative delay between the pump and Stokes pulses [22,27]. The pulse durations of the pump ( $\tau_p$ ) and Stokes ( $\tau_s$ ) at the sample level can then be calculated from the full width at half maximum (FWHM) of the SFG ( $W_{SFG}$ ) and FWM ( $W_{FWM}$ ) with the following equations:

$$\tau_p = \sqrt{2(W_{SFG}^2 - W_{FWM}^2)} \quad (1)$$

$$\tau_s = \sqrt{2W_{FWM}^2 - W_{SFG}^2} \quad (2)$$

The values for the measured and theoretically estimated pulse durations for the pump and Stokes beams are plotted in Fig. 1 (c) as a function of the propagation length inside the TIH53 glass blocks.

**Signal-to-Noise Ratio (SNR)** To determine the SNR of the system, a series of 20 images of a homogeneous sample was collected. The SNR of each frame was then determined by calculating the mean intensity of the central  $51 \times 51$ -pixel area (corresponding to 10% of the width of a  $512 \times 512$ -pixel image) and dividing by the standard deviation of the pixels [21]. Calculating the mean over the standard deviation in the central area mitigates the effects of variable intensity in different parts of the field of view. The SNR was averaged over all 20 frames to yield the reported SNR. The same materials (benzonitrile and DMSO) used in the spectral resolution measurement were used to determine the SNR. When collecting images, an average power of

50 mW was used in the pump and an average power of 30 mW was used in the Stokes. While reduced peak intensity at a higher number of bounces can be compensated with a higher laser power, the average powers were kept constant to compare the imaging properties of different numbers of bounces under the same conditions. The SNR reported here was determined as a function of the amount of dispersion introduced by the glass blocks. A comprehensive discussion of other factors such as the relative intensity noise of the laser affecting the value of the SNR in an SRS setup has been presented elsewhere [28] and is not reported in this paper.

**Spectral Resolution** To determine the spectral resolution, we first obtained an SRS spectrum of a sample with two adjacent characteristic Raman peaks. In the FP region, a benzonitrile sample with Raman peaks at 1001 and 1027  $\text{cm}^{-1}$  was used, while a DMSO sample with Raman peaks at 2914 and 2998  $\text{cm}^{-1}$  was used in the CH region. The SRS spectrum was obtained by varying the time delay between the pump and Stokes pulses. At each position of the delay line, an SRS image was obtained by scanning the galvanometer mirrors over the sample. The intensities of all the pixels in the resulting SRS image were summed up to provide the SRS intensity at that delay line position; this process was repeated for the whole scan range of the delay line. Once the SRS spectrum including both Raman peaks was obtained, the calibration of the delay line position in terms of the Raman shift in wavenumbers was obtained by comparing the known wavenumber difference between the two peaks and the observed delay line position difference. The spectral resolution was then determined from the FWHM of the higher-intensity peak in the SRS spectrum.

**Spatial Resolution** The transverse resolution of the system was estimated from an SRS image ( $1024 \times 1024$  pixels) of 0.6  $\mu\text{m}$  polystyrene beads wedged between two thin glass coverslips. ImageJ [29] software was used to measure the SRS intensity profile of a single bead. The FWHM of a Gaussian curve fit to the grayscale SRS intensity profile provided the transverse resolution. The axial resolution of the system was estimated from a 100-image  $128 \times 128$ -pixel z-stack (0.1  $\mu\text{m}$  spacing between images) which was then identically fitted to a Gaussian curve of the intensity profile of the beads.

## 2.4. Samples

The following calibration samples were used for the FP region: benzonitrile (1001 and 1027  $\text{cm}^{-1}$ ); oleic acid (1263 and 1301  $\text{cm}^{-1}$ ); paraffin (1441 and 1462  $\text{cm}^{-1}$ ); and acetaminophen (1614 and 1648  $\text{cm}^{-1}$ ). For the CH region, calibration samples used were DMSO (2914 and 2998  $\text{cm}^{-1}$ ) and polystyrene (2852 and 2904  $\text{cm}^{-1}$ ).

Formalin-fixed paraffin-embedded (FFPE) surgical prostate cancer tissues (radical prostatectomies) were used for the construction of tissue microarrays (TMAs) following approval by the local ethics review boards at the Centre Hospitalier de l'Université de Montréal (CHUM). The TMA sections on microscope glass slides were dewaxed using standard protocols and imaged with SRS using a 20X air objective.

Human epithelial breast tumor (MCF-7) cells were cultured in DMEM medium supplemented with 10% fetal bovine serum. Approximately  $5 \times 10^5$  MCF-7 cells were seeded onto 35 mm round glass-bottom dishes (MatTek). Cells were allowed to incubate for 24 hours post-seeding to achieve 50% confluency. The cells were irradiated using an X-ray irradiator (X-Rad320, Precision Xray) with 120 kVp X-rays. Half the cells were irradiated at 30 Gy (1 Gy/minute) while the other half were left unirradiated as a control group. The cell culture dishes were left in the incubator for 24 hours post-exposure. At each time point, the cells were chemically fixed using 4% paraformaldehyde and stored in distilled water at 4°C. Stimulated Raman scattering microscopy of the fixed cells was performed using a 40X (0.8 NA) water immersion objective.



### 3. Results

#### 3.1. SRS imaging system characterization as a function of chirp

We characterized the performance of our setup by determining the spectral resolution and SNR for a given number of bounces in the glass blocks. In the FP region, we characterized our setup for chirp values corresponding to 6–6 bounces, 7–7 bounces, and 8–8 bounces for the pump and Stokes. To determine the spectral resolution in the FP region, SRS imaging was conducted on a benzonitrile sample as described in Section 2 with a wavelength of 942 nm for the pump and 1040 nm for the Stokes, corresponding to a Raman shift of  $1001\text{ cm}^{-1}$ . Results are shown in Fig. 2(a) where the SRS spectrum for this Raman peak at different chirp values is compared with the corresponding spontaneous Raman spectrum with a linewidth of  $5.5\text{ cm}^{-1}$ . Due to the less stringent spectral resolution requirements for the CH region when compared to the FP region [30], we characterized our setup for the CH region at lower chirp values associated with 2–2 bounces, 3–3 bounces, and 4–4 bounces for the pump and Stokes. The spectral resolution in the CH region was obtained from SRS imaging of the  $2914\text{ cm}^{-1}$  Raman peak of the DMSO sample as mentioned in Section 2. When measuring the SNR, the average powers of the pump and Stokes lasers were kept constant to compare different numbers of bounces more effectively (Section 2). The performance results in the FP and CH regions for the experimentally determined pulse durations, SNRs, and spectral resolutions are summarized in Table 1. As expected, higher chirp values corresponding to a higher number of bounces lead to increasing spectral resolution but decreasing SNR. Figures 2(b) and 2(c) present the transverse view of an SRS image of  $0.6\text{ }\mu\text{m}$  polystyrene beads collected at 6–6 bounces in the FP region when imaged with the 40X (0.8 NA) water immersion microscope objective. As shown in Fig. 2(c) and 2(d), the SRS intensity profile of a single bead yielded a transverse resolution of  $0.7\text{ }\mu\text{m}$ . The system axial resolution was found to be  $\sim 5\text{ }\mu\text{m}$ . The spectral range covered using the 796 nm pump beam for the CH region, determined by measuring the FWHM of the two-photon absorption peak of rhodamine, was determined to be  $142\text{ cm}^{-1}$  (See Supplement 1).

**Table 1. Experimentally determined pulse durations, SNR, and spectral resolution for a given number of pump and Stokes bounces when performing SRS imaging in the FP and CH region. For 2 to 4 bounces, the pump wavelength is set to 796 nm, while for 6 to 8 bounces it is set to 942 nm.**

Number of bounces for pump and Stokes	Pump pulse duration at sample (ps)	Stokes pulse duration at sample (ps)	SNR	Spectral resolution ( $\text{cm}^{-1}$ )
<i>CH-stretching region</i>				
2	1.10	0.78	310	29.6
3	1.64	0.92	280	24.4
4	2.08	1.10	210	22.9
<i>Fingerprint region</i>				
6	2.50	1.32	77	12.3
7	2.97	1.56	67	11.3
8	3.37	1.79	53	10.5

#### 3.2. SRS imaging of biological samples in the FP and CH regions at optimal chirp

To illustrate the imaging capabilities of the system, we applied our setup to imaging biological samples. We evaluated the performance in the FP region by recording SRS images of prostate cancer tissues. Prostate cancer (PC) is the most diagnosed cancer in North American men. In

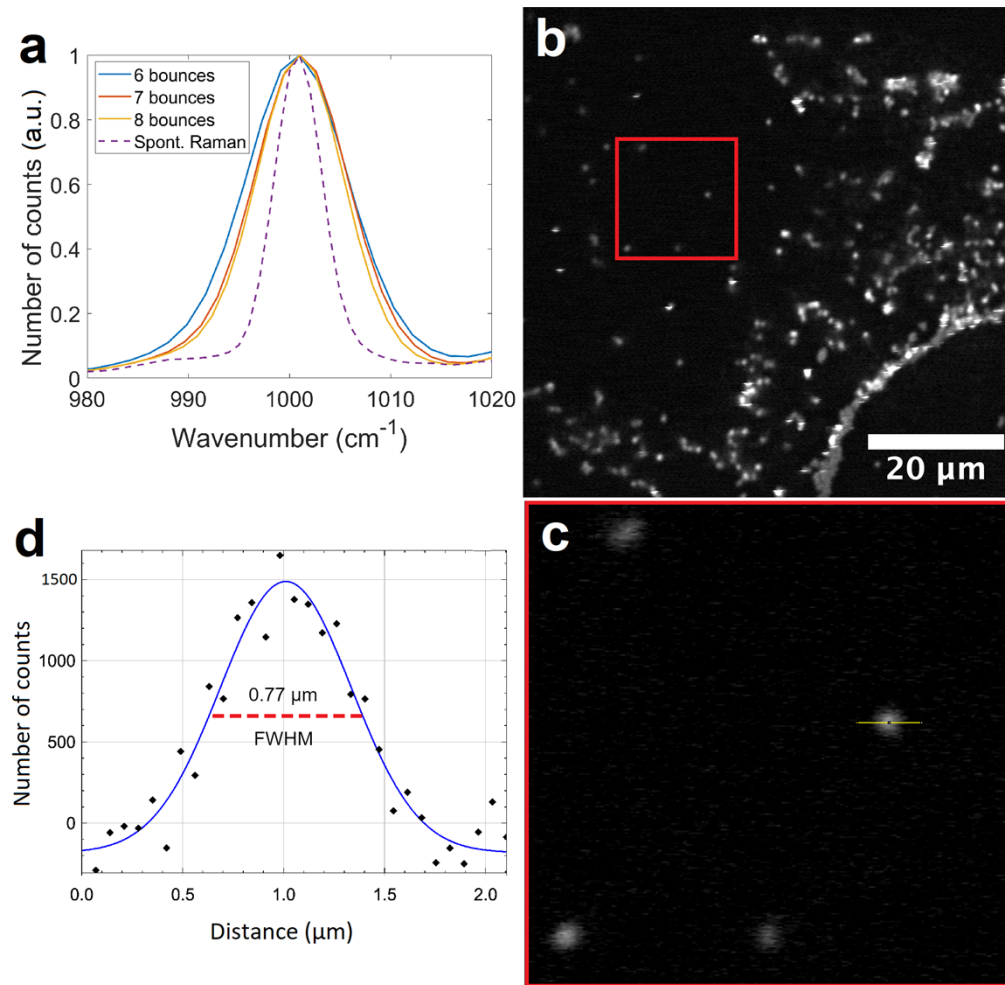


**Fig. 2.** Characterization measurements for SRS microscope in the FP region. (a) SRS spectral profile of the benzonitrile Raman band at  $1001\text{ cm}^{-1}$  for 6–6 (6 for the pump and Stokes each), 7–7, and 8–8 bounces in the FP region alongside the corresponding spontaneous Raman spectrum. (b) SRS image of  $0.6\text{ }\mu\text{m}$  polystyrene beads at the  $1004\text{ cm}^{-1}$  Raman band. (c) Zoom-in of the highlighted region in the SRS image shown in (a). (d) Measured and fitted (solid line) transverse SRS intensity profile associated with a single  $0.6\text{ }\mu\text{m}$  polystyrene bead. A FWHM value of  $0.7\text{ }\mu\text{m}$  is obtained for the transverse resolution. The pixels analyzed in this curve are shown in (c) as a yellow line.

particular, intraductal carcinoma of the prostate (IDC-P) is an aggressive variant of PC that is associated with PC recurrence and poor prognosis [31]. Recent work involving Raman microspectroscopy [32] identified Raman biomarker bands at  $1004$ ,  $1250$ ,  $1477$ , and  $1644\text{ cm}^{-1}$  that correlated with the presence of IDC-P and corresponded to contributions from proteins, DNA/RNA, and lipids. The goal of our study is to determine whether features extracted from SRS images of PC tissue at these Raman bands can be useful for the high-throughput identification of IDC-P. Table 1 shows that 6 bounces for the pump and Stokes provide the best SNR in the FP region while maintaining sufficient spectral resolution to image the targeted Raman bands. Hence 6 bounces for the pump and Stokes were used for generating spectrally focused SRS images. We first performed a calibration of the Raman shift as a function of delay line position

to target the required Raman bands in the PC tissue, using samples of benzonitrile, oleic acid, paraffin, and acetaminophen (Fig. 3(a)). The SRS images (average of 10 frames) of PC tissue at 1004, 1250, 1477, and 1644  $\text{cm}^{-1}$  seen in Fig. 3 (b–e) seem to reveal only subtle intensity variations across the different bands over the field of view. To better visualize the variations in each image, a co-registered image can be produced where each prostate image at a given Raman band is normalized, assigned a pseudo color, and combined into a single image.

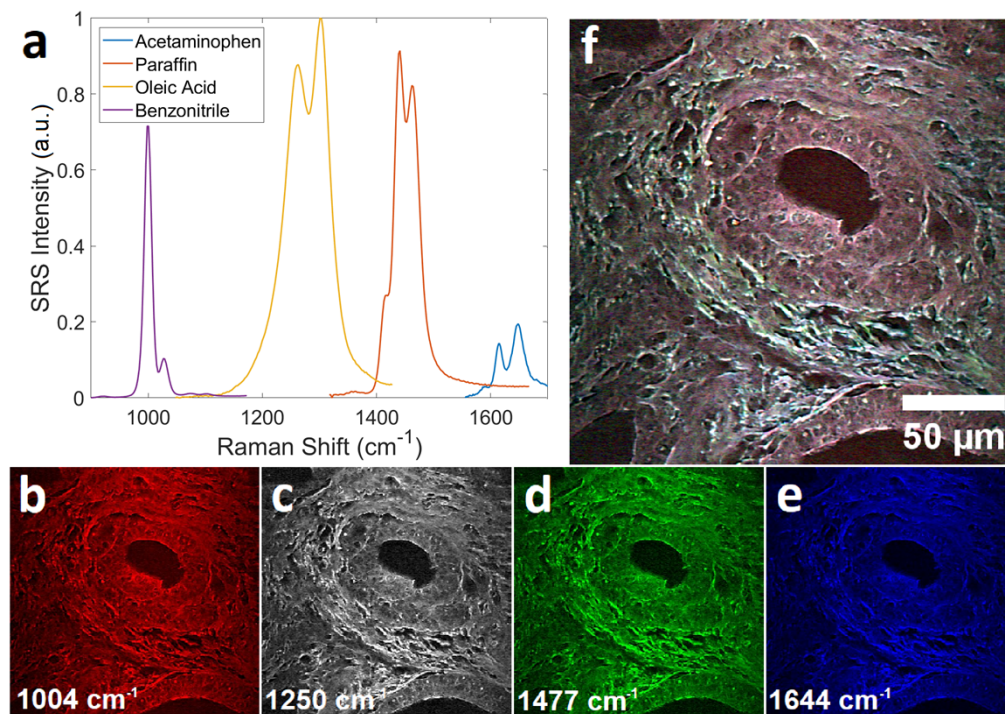


**Fig. 3.** SRS imaging of PC tissue. Images were collected at  $512 \times 512$  pixels with an integration time of 20  $\mu\text{s}$  for a total acquisition time of 5.2 seconds per image. (a) SRS spectra of benzonitrile, oleic acid, paraffin, and acetaminophen. SRS images of PC tissue when using 6 bounces for pump and Stokes at the Raman bands of (b) 1004  $\text{cm}^{-1}$ , (c) 1250  $\text{cm}^{-1}$ , (d) 1477  $\text{cm}^{-1}$ , and (e) 1644  $\text{cm}^{-1}$ . (f) Co-registered image of SRS PC tissue at the Raman bands corresponding to 1004  $\text{cm}^{-1}$  (red), 1477  $\text{cm}^{-1}$  (green), and 1644  $\text{cm}^{-1}$  (blue).

The co-registered SRS image (Fig. 3(f)) suggests location-specific differences in the chemical constituents. This illustrates the high-spectral resolution capability of our setup to perform SRS imaging in the spectrally dense FP region. Our ongoing work involves the implementation of i) frequency-modulated SRS [5,33] to reduce the contributions of the two-photon absorption background that may be confounding the SRS signal, and ii) the Stokes beam amplification [34] to improve the SNR in the FP region.

Next, we explored the application of SRS imaging in the CH region to visualize the response of human epithelial breast cancer (MCF-7) cells exposed to ionizing radiation. Radiation therapy (RT) is a standard treatment utilizing X-rays to treat breast cancer. However, a mechanistic understanding of the heterogeneity of sub-cellular response to RT is particularly lacking at present [35]. Our goal for this work is to investigate the potential of SRS imaging in the CH region to determine biomarkers of radiobiological response. We imaged both unirradiated (0 Gy) and irradiated (30 Gy) MCF-7 cells at the 2926  $\text{cm}^{-1}$  ( $\text{CH}_2$ ,  $\text{CH}_3$ ) band with overlapping contributions



from proteins, lipids, and DNA and the  $2850\text{ cm}^{-1}$  ( $\text{CH}_2$ ) band with contributions predominantly from lipids. As seen in Table 1, 2–2 bounces in the CH region, provided the best SNR while maintaining sufficient spectral resolution to image the targeted Raman bands. A calibration of the Raman shift as a function of delay line position to target the required Raman bands was performed using DMSO and polystyrene calibration samples. The SRS images (average of 10 frames) at Raman shifts of  $2850$  and  $2926\text{ cm}^{-1}$  of chemically fixed MCF-7 cells are shown in Fig. 4 at 24 hours-post exposure to 0 Gy (not irradiated; Fig. 4(a)–4(c)) and 30 Gy (Fig. 4(d)–4(f)). Most prominently, the cell nuclei appear darker in the lipid band images at  $2850\text{ cm}^{-1}$  (Fig. 4(a) and 4(d)) as expected. In contrast, whole cells with clearly visible nuclei and nucleoli are seen in the SRS image at  $2926\text{ cm}^{-1}$ . Consistent with the impact on the survival fraction after X-ray exposure [36], fewer MCF-7 cells with a flat enlarged cell morphology are evident at 30 Gy (Fig. 4(d)–4(f)). Our ongoing work is aimed at characterizing this radiobiological response over a wide dose range and over multiple time points.

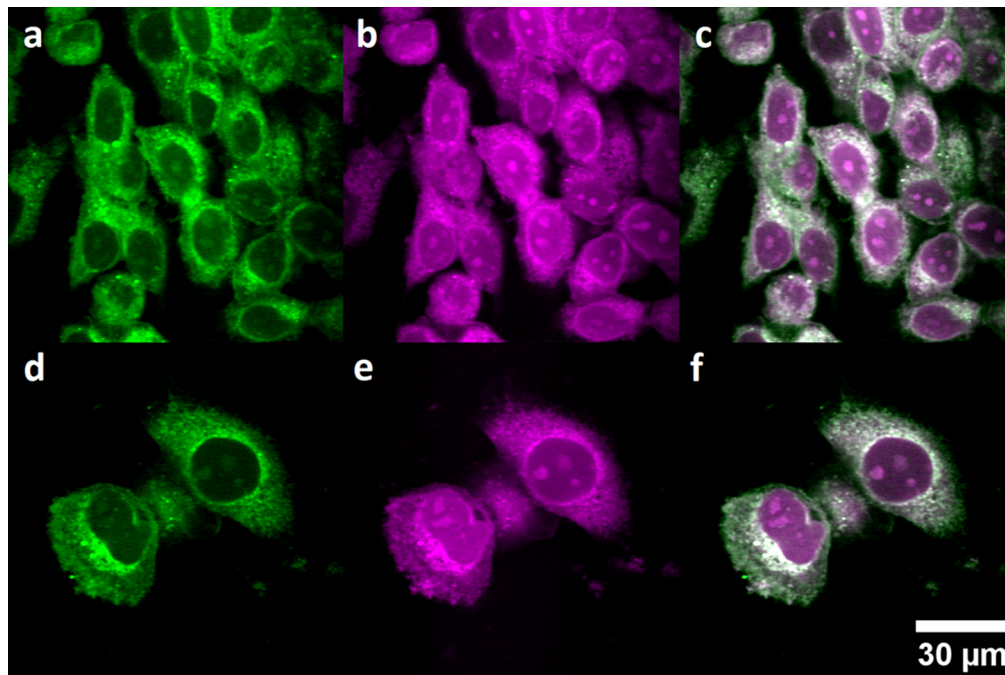


**Fig. 4.** SRS imaging of MCF-7 cells at 24 hours-post exposure to X-ray radiation with 2 bounces each in the TIH53 glass blocks for the pump and Stokes beams. Images were collected at  $512 \times 512$  pixels with an integration time of  $20\text{ }\mu\text{s}$  for a total acquisition time of 5.2 seconds per image. Images of unirradiated (0 Gy) MCF-7 cells at the (a)  $2850\text{ cm}^{-1}$  and (b)  $2926\text{ cm}^{-1}$  bands. (c) A co-registered image of the 0 Gy images, with the  $2850\text{ cm}^{-1}$  image in green and the  $2926\text{ cm}^{-1}$  image in purple. Images of MCF-7 cells irradiated with 30 Gy at (d)  $2850\text{ cm}^{-1}$  and (e)  $2926\text{ cm}^{-1}$ . (f) A co-registered image of the 30 Gy images, with the same color scheme as in (c).

#### 4. Discussion

In this work, we demonstrated a spectral focusing SRS imaging system that uses adjustable-dispersion TIH53 glass blocks to quickly adjust the chirp of the excitation pulses. In both the FP and CH regions, the pulse duration of the pump and Stokes pulses increased as a function of the number of bounces in the glass blocks (Fig. 1(c)). This observation confirms that the pulse

duration and the quantity of chirp in the pump and Stokes pulses increase as a function of the distance propagated in TIH53 glass as expected. Furthermore, our experimentally determined pulse duration values are consistent with the theoretical predictions ([Supplement 1](#)), with a discrepancy of 5–35% between the experimental and theoretical values. This difference can be attributed to uncertainty in the autocorrelator measurement which yielded the transform-limited pulse width of the laser pulses used to estimate the theoretical values. This is likely due to the laser pulses directly out of the laser not being transform-limited owing to internal dispersion compensation.

We further quantified the performance of the setup by imaging homogeneous samples (Benzonitrile and DMSO) in the FP and CH regions for a different number of bounces in the glass blocks for the pump and Stokes and summarized in our results in [Table 1](#). Because broader pulses have lower peak energies, the SNR of the system in both the FP and CH regions decreased as expected when the pulse chirp was increased. Also consistent with expectations, the spectral resolution increased as the number of bounces increased in the FP and CH regions. Notably, using a higher number of bounces showed diminishing returns on the increase in spectral resolution, especially in the case of the CH region, where an increase from 2 to 3 bounces yielded a 21% increase in spectral resolution (29.6 to 24.4  $\text{cm}^{-1}$ ), while an increase from 3 to 4 bounces only yielded a 6.5% increase (24.4 to 22.9  $\text{cm}^{-1}$ ). This is most likely due to the increasing chirp mismatch between the pump and Stokes as the number of bounces increases (See [Supplement 1](#)). The current study compared SNR values with constant average laser power to obtain the best relative comparison between different numbers of bounces. The choice of the average laser power in an experiment will depend on the photodamage threshold of the sample being imaged. With the current glass blocks, the chirp can only be modulated in chirp increments of 10 cm of propagation in TIH53 glass, which makes some chirp mismatch inevitable. A second chirping mechanism capable of modulating the chirp within the GDD provided by 10 cm of glass would allow the system to perfectly match the chirp of the pump and Stokes when using the glass blocks. One possible solution would be an identical but thinner glass block capable of modulating the chirp in steps of 1 cm of TIH53 glass, which addresses this problem without compromising the ease of alignment of the system.

The average power transmission through the glass blocks for the first two bounces was experimentally determined to be  $\sim 65\%$ . However, subsequent optical transmission throughout the glass block is nearly lossless with transmissions of 99.6% at 796 nm, 99.8% at 942 nm, and 99.9% at 1040 nm for each bounce. The power loss of the pump and Stokes is attributed to damage in the silver coating at the location of the first two reflections and will be eliminated by re-coating the silver surface. Such optical damage can be prevented in the future by avoiding focusing the laser beams on the silver coating while aligning the telescope in front of the glass block.

In the optical setup used in this work, the pump and Stokes pulses can be chirped up to a few picoseconds (e.g. 4.5 ps at 796 nm) due to the size limitation of the glass blocks. However, experiments that require even longer pulses [[37](#)] can make use of adjustable-dispersion glass blocks by either increasing the length of the glass block to increase the path length per bounce or by increasing the width of the glass blocks to increase the maximum possible number of bounces. More generally, the dimensions of the glass blocks can be chosen to suit how broadly the user wishes to tune their specific setup. The chirp values in this work were closely matched by using the same number of bounces in two different glass blocks for the pump and Stokes beams. However, in some cases, improved chirp-matching is possible by using an unequal number of bounces in the two glass blocks, provided that a sufficiently long delay line is used to accommodate the corresponding path length difference. On the other hand, using the same number of bounces and a single glass block to propagate both pump and Stokes beams will be advantageous for future development of a compact miniaturized setup. When looking at the collective effects on the pulse

duration, the SNR, and the spectral resolution, we can confirm the fundamental principle of the glass blocks: the glass blocks allow the user to make a tradeoff between the SNR and the spectral resolution of the system to suit the user's imaging requirements. For example, as discussed in Section 3.2, the optimal chirp was provided by 6 and 2 bounces respectively for the FP and CH region. We demonstrated the high-spectral resolution imaging capabilities of our setup for this selection of bounces by imaging PC tissue in the FP region (Fig. 3) and MCF-7 cells in the CH region (Fig. 4). In the prostate core tissue, the co-registered SRS image revealed subtle intensity variations across the different Raman bands at 1004, 1477, and 1644  $\text{cm}^{-1}$ . These variations suggested location-specific differences in the chemical constituents that will be investigated in ongoing work. In the SRS images of MCF-7 cells, clear differences are apparent between the lipid contributions at 2850  $\text{cm}^{-1}$  and the mixed contributions from proteins, lipids, and DNA at 2926  $\text{cm}^{-1}$ . Our recent investigations using this SRS imaging platform in the CH region have revealed interesting chemical and morphological differences between control and 30 Gy irradiated MCF-7 cells [38].

## 5. Conclusion

In summary, we have presented a spectral focusing SRS system capable of quickly modulating the chirp of its pump and Stokes pulses by using TIH53 adjustable-dispersion glass blocks. With a large GDD and a minimal TOD, these glass blocks enable our setup to conveniently adjust its SNR and spectral resolution to image bands in the FP and CH regions. To demonstrate this flexibility, we showed a capability of varying the spectral resolution from 10.5 to 29.6  $\text{cm}^{-1}$ , with a corresponding SNR variation of 53 to 310. We then illustrated how these settings could be used to image prostate cores in the FP region as well as MCF-7 cells in the CH region without needing to significantly realign the system. These glass blocks can be conveniently installed in any SRS configuration implementing spectral focusing. We believe the compactness and simplicity of the glass blocks have the potential to make spectral focusing more viable for clinical applications.

**Funding.** Fonds de Recherche du Québec - Santé; Canada Foundation for Innovation and Tier I Canada Research Chair; Canadian Institutes of Health Research (PJT-169164); Natural Sciences and Engineering Research Council of Canada (RGPIN-2022-04897).

**Acknowledgments.** We acknowledge the help of Prof. Edana Cassol, Robyn Skilling, Dr. Duale Ahmed, Prof. William Willmore, and Prof. Martin Holcik at Carleton University for samples of MCF-7 cells. We thank Sarita Cuadros Sanchez, Kaitlyn Altwasser, and Dr. Vinita Chauhan at Health Canada for help with the irradiation of cells. Our sincere thanks to Prof. Dan Fu and his team at the University of Washington, Seattle for helpful discussions related to the spectral focusing-based SRS setup. We thank the molecular pathology core facility of the CRCHUM for preparing sections. Biobanking at the CRCHUM, CHUQc-UL, and MUHC was done in collaboration with the Réseau de Recherche sur le cancer of the Fonds de Recherche Québec - Santé (FRQS).

**Disclosures.** The authors declare no conflicts of interest.

**Data availability.** Data underlying the results presented in this paper are not publicly available at this time but may be obtained from the authors upon reasonable request.

**Supplemental document.** See [Supplement 1](#) for supporting content.

## References

1. A. H. Hill and D. Fu, "Cellular Imaging Using Stimulated Raman Scattering Microscopy," *Anal. Chem.* **91**(15), 9333–9342 (2019).
2. F. Hu, L. Shi, and W. Min, "Biological imaging of chemical bonds by stimulated Raman scattering microscopy," *Nat. Methods* **16**(9), 830–842 (2019).
3. D. A. Orringer, B. Pandian, and Y. S. Niknafs, *et al.*, "Rapid intraoperative histology of unprocessed surgical specimens via fibre-laser-based stimulated Raman scattering microscopy," *Nat. Biomed. Eng.* **1**(2), 0027 (2017).
4. B. Sarri, R. Canonge, X. Audier, E. Simon, J. Wojak, F. Caillol, C. Cadot, D. Marguet, F. Poizat, M. Giovanni, and H. Rigneault, "Fast stimulated Raman and second harmonic generation imaging for intraoperative gastro-intestinal cancer detection," *Sci. Rep.* **9**(1), 10052 (2019).
5. D. Fu, W. Yang, and X. S. Xie, "Label-free imaging of neurotransmitter acetylcholine at neuromuscular junctions with stimulated Raman scattering," *J. Am. Chem. Soc.* **139**(2), 583–586 (2017).

6. J. Li, S. Condello, J. Thomes-Pepin, X. Ma, Y. Xia, T. D. Hurley, D. Matei, and J. Cheng, "Lipid Desaturation Is a Metabolic Marker and Therapeutic Target of Ovarian Cancer Stem Cells," *Cell Stem Cell* **20**(3), 303–314.e5 (2017).
7. J. Du, Y. Su, C. Qian, D. Yuan, K. Miao, D. Lee, A. H. C. Ng, R. S. Wijker, A. Ribas, R. D. Levine, J. R. Heath, and L. Wei, "Raman-guided subcellular pharmacometabolomics for metastatic melanoma cells," *Nat. Commun.* **11**(1), 4830 (2020).
8. B. G. Saar, C. W. Freudiger, J. Reichman, C. M. Stanley, G. R. Holtom, and X. S. Xie, "Video-rate molecular imaging in vivo with stimulated Raman scattering," *Science* **330**(6009), 1368–1370 (2010).
9. F. K. Lu, S. Basu, V. Igras, M. P. Hoang, M. Ji, D. Fu, G. R. Holtom, V. A. Neel, C. W. Freudiger, D. E. Fisher, and X. S. Xie, "Label-free DNA imaging in vivo with stimulated Raman scattering microscopy," *Proc. Natl. Acad. Sci. U. S. A.* **112**(37), 11624–11629 (2015).
10. P. Lin, H. Ni, H. Li, N. A. Vickers, Y. Tan, R. Gong, T. Bifano, and J. Cheng, "Volumetric chemical imaging in vivo by a remote-focusing stimulated Raman scattering microscope," *Opt. Express* **28**(20), 30210 (2020).
11. Y. Ozeki, W. Umemura, Y. Otsuka, S. Satoh, H. Hashimoto, K. Sumimura, N. Nishizawa, K. Fukui, and K. Itoh, "High-speed molecular spectral imaging of tissue with stimulated Raman scattering," *Nat. Photonics* **6**(12), 845–851 (2012).
12. J. Réhault, F. Crisafi, V. Kumar, G. Ciardi, M. Marangoni, G. Cerullo, and P. Polli, "Broadband stimulated Raman scattering with Fourier-transform detection," *Opt. Express* **23**(19), 25235 (2015).
13. D. Fu, G. Holtom, C. Freudiger, X. Zhang, and X. S. Xie, "Hyperspectral imaging with stimulated Raman scattering by chirped femtosecond lasers," *J. Phys. Chem. B* **117**(16), 4634–4640 (2013).
14. H. Lin, H. J. Lee, N. Tague, J. B. Lugagne, C. Zong, F. Deng, J. Shin, L. Tian, W. Wong, M. J. Dunlop, and J. Cheng, "Microsecond fingerprint stimulated Raman spectroscopic imaging by ultrafast tuning and spatial-spectral learning," *Nat. Commun.* **12**(1), 3052 (2021).
15. T. Hellerer, A. M. K. Enejder, and A. Zumbusch, "Spectral focusing: High spectral resolution spectroscopy with broad-bandwidth laser pulses," *Appl. Phys. Lett.* **85**(1), 25–27 (2004).
16. K. P. Knutsen, B. M. Messer, R. M. Onorato, and R. J. Saykally, "Chirped coherent anti-Stokes Raman scattering for high spectral resolution spectroscopy and chemically selective imaging," *J. Phys. Chem. B* **110**(12), 5854–5864 (2006).
17. W. Langbein, I. Rocha-Mendoza, and P. Borri, "Coherent anti-Stokes Raman micro-spectroscopy using spectral focusing: Theory and experiment," *J. Raman Spectrosc.* **40**(7), 800–808 (2009).
18. R. A. Cole and A. D. Slepov, "Interplay of pulse bandwidth and spectral resolution in spectral-focusing CARS microscopy," *J. Opt. Soc. Am. B* **35**(4), 842 (2018).
19. M. Mohseni, C. Polzer, and T. Hellerer, "Resolution of spectral focusing in coherent Raman imaging," *Opt. Express* **26**(8), 10230 (2018).
20. T. Ito, Y. Obara, and K. Misawa, "Invited Article: Spectral focusing with asymmetric pulses for high-contrast pump-probe stimulated Raman scattering microscopy," *APL Photonics* **3**(9), 092405 (2018).
21. R. Espinoza, B. Wong, and D. Fu, "Real-time, Two-color Stimulated Raman Scattering Imaging of Mouse Brain for Tissue Diagnosis," *J. Visualized Exp.* **1**(180), 1 (2022).
22. C. Brideau, Polarization Controlled Coherent Anti-Stokes Raman Scattering Microscopy for Determination of Structural Order of the Myelin Sheath. (2018).
23. C. Brideau, K. W. C. Poon, P. Colarusso, and P. K. Stys, "Excitation parameters optimized for coherent anti-Stokes Raman scattering imaging of myelinated tissue," *J. Biomed. Opt.* **24**(04), 1 (2019).
24. A. F. Pegoraro, A. Ridsdale, D. J. Moffatt, Y. Jia, J. P. Pezacki, and A. Stolow, "Optimally chirped multimodal CARS microscopy based on a single Ti:sapphire oscillator," *Opt. Express* **17**(4), 2984–2996 (2009).
25. C. H. Allen, B. Hansson, O. Raiche-Tanner, and S. Murugkar, "Coherent anti-Stokes Raman scattering imaging using silicon photomultipliers," *Opt. Lett.* **45**(8), 2299 (2020).
26. T. A. Pologruto, B. L. Sabatini, and K. Svoboda, "ScanImage: Flexible software for operating laser scanning microscopes," <http://www.biomedical-engineering-online.com/content/2/1/13> (2003).
27. V. Piazza, G. de Vito, E. Farrokhtakin, G. Ciofani, and V. Mattoli, "Femtosecond-laser-pulse characterization and optimization for CARS Microscopy," *PLoS One* **11**(5), e0156371 (2016).
28. X. Audier, S. Heuke, P. Volz, I. Rimke, and H. Rigneault, "Noise in stimulated Raman scattering measurement: From basics to practice," *APL Photonics* **5**(1), 011101 (2020).
29. C. A. Schneider, W. S. Rasband, and K. W. Eliceiri, "NIH Image to ImageJ: 25 years of Image Analysis HHS Public Access," *Nat. Methods* **9**(7), 671 (2012).
30. J. X. Cheng, A. Volkmer, L. D. Book, and X. S. Xie, "Epi-detected coherent anti-Stokes Raman scattering (E-CARS) microscope with high spectral resolution and high sensitivity," *J. Phys. Chem. B* **105**(7), 1277–1280 (2001).
31. H. Pantazopoulos, M. K. Diop, A. A. Grosset, F. Rouleau-Gagné, A. Al-Saleh, T. Boblea, and D. Trudel, "Intraductal Carcinoma of the Prostate as a Cause of Prostate Cancer Metastasis: A Molecular Portrait," *Cancers* **14**(3), 820 (2022).
32. A. A. Grosset, F. Dallaire, and T. Nguyen, *et al.*, "Identification of intraductal carcinoma of the prostate on tissue specimens using Raman micro-spectroscopy: A diagnostic accuracy case-control study with multicohort validation," *PLoS Med.* **17**(8), e1003281 (2020).
33. H. Xiong, N. Qian, Z. Zhao, L. Shi, Y. Miao, and W. Min, "Background-free imaging of chemical bonds by a simple and robust frequency-modulated stimulated Raman scattering microscopy," *Opt. Express* **28**(10), 15663 (2020).



34. B. Figueroa, W. Fu, T. Nguyen, K. Shin, B. Manifold, F. Wise, and D. Fu, "Broadband hyperspectral stimulated Raman scattering microscopy with a parabolic fiber amplifier source," *Biomed. Opt. Express* **9**(12), 6116 (2018).
35. R. Baskar, J. Dai, N. Wenlong, R. Yeo, and K. W. Yeoh, "Biological response of cancer cells to radiation treatment," *Front. Mol. Biosci.* **1**, 24 (2014).
36. S. Adjemian, T. Oltean, S. Martens, B. Wiernicki, V. Goossens, T. Vanden Berghe, B. Cappe, M. Ladik, F. B. Riquet, L. Heyndrickx, J. Bridelance, M. Vuylsteke, K. Vandecasteele, and P. Vandenabeele, "Ionizing radiation results in a mixture of cellular outcomes including mitotic catastrophe, senescence, methuosis, and iron-dependent cell death," *Cell Death Dis.* **11**(11), 1003 (2020).
37. K. Koike, N. I. Smith, and K. Fujita, "Spectral focusing in picosecond pulsed stimulated Raman scattering microscopy," *Biomed. Opt. Express* **13**(2), 995 (2022).
38. C. H. Allen, R. Skilling, D. Ahmed, S. C. Sanchez, K. Altwasser, J. R. Gagnon, V. Chauhan, E. Cassol, and S. Murugkar, "Imaging radiobiological response of breast cancer cells in vitro using stimulated Raman scattering," *Proc. SPIE, Advanced Chemical Microscopy for Life Science and Translational Medicine 2023* (2023).